

# Band structures and $\mathbb{Z}_2$ invariants of 2D transition metal dichalcogenide monolayers from fully-relativistic Dirac–Kohn–Sham theory using Gaussian-type orbitals

Marius Kadek,<sup>1,2,3,\*</sup> Baokai Wang,<sup>1</sup> Marc Joosten,<sup>2</sup> Wei-Chi Chiu,<sup>1</sup>  
Francois Mairesse,<sup>4</sup> Michal Repisky,<sup>2,5</sup> Kenneth Ruud,<sup>2</sup> and Arun Bansil<sup>1</sup>

<sup>1</sup>*Department of Physics, Northeastern University, Boston, Massachusetts 02115, USA*

<sup>2</sup>*Hylleraas Centre for Quantum Molecular Sciences,*

*UiT The Arctic University of Norway, N-9037 Tromsø, Norway*

<sup>3</sup>*Algorithmiq Ltd., Kanavakatu 3C, FI-00160 Helsinki, Finland*

<sup>4</sup>*Laboratory of Theoretical Chemistry, University of Namur, B-5000 Namur, Belgium*

<sup>5</sup>*Department of Physical and Theoretical Chemistry,  
Faculty of Natural Sciences, Comenius University, Bratislava, Slovakia*

(Dated: February 2, 2023)

Two-dimensional (2D) materials exhibit a wide range of remarkable phenomena, many of which owe their existence to the relativistic spin–orbit coupling (SOC) effects. To understand and predict properties of materials containing heavy elements, such as the transition-metal dichalcogenides (TMDs), relativistic effects must be taken into account in first-principles calculations. We present an all-electron method based on the four-component Dirac Hamiltonian and Gaussian-type orbitals (GTOs) that overcomes complications associated with linear dependencies and ill-conditioned matrices that arise when diffuse functions are included in the basis. Until now, there has been no systematic study of the convergence of GTO basis sets for periodic solids either at the nonrelativistic or the relativistic level. Here we provide such a study of relativistic band structures of the 2D TMDs in the hexagonal (2H), tetragonal (1T), and distorted tetragonal (1T') structures, along with a discussion of their SOC-driven properties (Rashba splitting and  $\mathbb{Z}_2$  topological invariants). We demonstrate the viability of our approach even when large basis sets with multiple basis functions involving various valence orbitals (denoted triple- and quadruple- $\zeta$ ) are used in the relativistic regime. Our method does not require the use of pseudopotentials and provides access to all electronic states within the same framework. Our study paves the way for direct studies of material properties, such as the parameters in spin Hamiltonians, that depend heavily on the electron density near atomic nuclei where relativistic and SOC effects are the strongest.

## I. INTRODUCTION

Two-dimensional (2D) materials [1, 2] are solids in which atoms or compounds are bound together by strong bonds (*e.g.* covalent or ionic) along two spatial dimensions, confining electron transport to a plane. In the out-of-plane dimension, weaker (van der Waals) forces enable the synthesis of materials with thicknesses of only a few atomic layers [3–6]. 2D materials have recently become very attractive as they exhibit a number of remarkable transport [7, 8], topological [9–11], thermoelectric [12], and optoelectronic [13] properties that can be exploited to develop novel devices for quantum computing [14, 15], field-effect transistors [16, 17], low-power logic devices [18], and strain-controllable light-emitting devices [19]. Advantages of 2D materials over conventional solids stem from their thin surfaces which enable considerable manipulation of their properties that can be controlled using defects, adatoms, and electric-field gating [20–22]. In addition, atomically thin materials can be manually assembled to form multilayered heterostructures [11, 17, 23, 24] to combine functionalities of individual layers [25].

Monolayers of the transition-metal dichalcogenides

(TMDs) [26] are 2D materials of type  $\text{MX}_2$ , where M is a transition-metal atom (Mo, W, ...), and X is a chalcogen atom (S, Se, Te), and constitute basic building blocks for many heterostructures. TMDs have been found to host a number of exotic physical phenomena, such as the quantum spin Hall (QSH) [11] and nonlinear anomalous Hall [27] effects, higher-order topology [28], giant Rashba spin-splittings of valence bands [29], as well as various correlated phases, *e.g.* charge density waves [30, 31], superconductivity and ferromagnetism [32]. TMDs typically contain elements from the lower part of the periodic table, where the relativistic theory of electrons is unavoidable. Many interesting properties of the TMDs owe their existence to the relativistic link between the spin and orbital degrees of freedom, *i.e.* the spin–orbit coupling (SOC) effects. The ability to control and tune SOC in TMDs opens new possibilities for spintronics and valleytronics devices based on non-magnetic materials, where spin is manipulated by electric means only [33–36]. Furthermore, SOC generates opposite effective Zeeman fields at the K and K' valleys of the TMDs, which enables formation of Cooper pairs and opens the possibility of observing topological superconductivity and Majorana fermions [37, 38]. Recently, antisite defects in TMDs were proposed to be suitable for hosting solid-state spin qubits, where SOC enables transitions between different spin configurations required for qubit operations [39].

\* [marius.kadek@uit.no](mailto:marius.kadek@uit.no)

First-principles computational approaches enable systematic parameter-free material-specific predictions in novel materials. However, due to the presence of heavy elements in the TMDs, it is important that relativistic and SOC effects are accounted for in the theoretical framework. In this connection, the four-component (4c) Dirac Hamiltonian [40–42]

$$\hat{H} = \begin{pmatrix} V(\mathbf{r}) & c\boldsymbol{\sigma} \cdot \boldsymbol{\pi} \\ c\boldsymbol{\sigma} \cdot \boldsymbol{\pi} & V(\mathbf{r}) - 2c^2 \end{pmatrix}, \quad (1)$$

is the commonly accepted gold standard due being exact in the limit of noninteracting relativistic electrons. Here,  $\boldsymbol{\sigma}$  are the Pauli matrices,  $\boldsymbol{\pi} \equiv -i\nabla + \mathbf{A}$  is the canonical momentum operator of the electron,  $c$  is the speed of light, and atomic units ( $e = \hbar = m_e = 1$ ) are used. The scalar and vector potentials  $V$  and  $\mathbf{A}$ , respectively, describe the interaction of the electron with external electromagnetic fields;  $V$  typically contains interactions with nuclear charges. The lower components of the Dirac bispinor wave functions are associated with the negative-energy states, and various strategies for their elimination lead to a number of approximate two-component (2c) schemes [43, 44].

The multiple wave-function components needed in relativistic simulations significantly increase the computational cost as larger matrix and vector dimensions are involved. Kohn–Sham (KS) density functional theory (DFT) [45, 46] brings relativistic calculations to an affordable level and remains the method of choice for large solid-state systems containing heavy elements. However, we note the work of Yeh *et al.* [47] on the self-consistent *GW* method at the relativistic 2c level of theory. In KS theory, the potential in Eq. (1) also contains terms that depend on the electron density and its gradient: the mean-field Coulomb potential generated by other electrons, and the exchange–correlation potential [41, 48–51]. The relativistic corrections to the instantaneous electron–electron Coulomb interactions are here neglected. If SOC is treated self-consistently, expensive KS Hamiltonian matrix constructions must be carried out in the multicomponent regime. As a consequence, most internal parts of quantum mechanical codes must be reconsidered and adapted. A transparent theoretical formalism that isolates the SOC terms, reduces computational cost, and simplifies the implementation of fully relativistic theories, can be achieved using quaternion algebra [52–55].

The most commonly applied strategies incorporate SOC in relativistic pseudopotentials and the related projector-augmented wave methods [56–60], where the oscillating wave function with complicated nodal structure in the core region close to the nuclei is replaced by a smooth pseudo-wavefunction. However, all-electron approaches are necessary to describe Rashba-like spin-splitting induced by distortions of the wave function close to nucleus [61], when nuclear spins interact with the electrons [62], or in situations where high accuracy is desired [63, 64]. Linearized augmented plane-wave [65–67] and full-potential linear muffin-tin orbital [68–70]

methods enable all-electron calculations by constructing muffin-tin spheres around all atoms and expressing the all-electron wave functions using orbitals inside these spheres and plane waves in the interstitial region. In such cases, treatment of SOC must be handled separately in the two distinct regions and is sometimes neglected outside of the muffin-tin spheres.

Our goal is to provide an alternative approach for modelling heavy-element-containing 2D materials and their properties. The technique is based on expanding the 4c Bloch wave functions  $\psi_n(\mathbf{k}; \mathbf{r})$  using linear combinations of atom-centered real-space bispinor basis functions  $\chi_\mu(\mathbf{r})$ :

$$\psi_n(\mathbf{k}; \mathbf{r}) = \frac{1}{\sqrt{|\mathcal{K}|}} \sum_{\mathbf{R}, \mu} e^{i\mathbf{k} \cdot \mathbf{R}} \chi_\mu(\mathbf{r} - \mathbf{R}) c_n^\mu(\mathbf{k}), \quad (2)$$

where  $n$  is the band index,  $\mathbf{k}$  is the reciprocal-space vector (quasi-momentum),  $\mathbf{R}$  denotes the Bravais lattice vector of the respective unit cell in the translationally invariant system ( $\mathbf{R} = \mathbf{0}$  is the reference unit cell), index  $\mu$  runs over the scalar basis functions in the unit cell, and the normalization constant is the inverse square root of the volume of the primitive reciprocal unit cell  $|\mathcal{K}|$ . The expansion coefficients  $c_n^\mu(\mathbf{k})$  and the ground-state electronic structure are obtained by solving the matrix form of the reciprocal-space Dirac–Kohn–Sham (DKS) generalized eigenvalue equation

$$H(\mathbf{k})c(\mathbf{k}) = S(\mathbf{k})c(\mathbf{k})\varepsilon(\mathbf{k}), \quad (3)$$

where  $\varepsilon(\mathbf{k})$  is the diagonal matrix of eigenvalues (band energies), and  $H(\mathbf{k})$  and  $S(\mathbf{k})$  are the reciprocal-space DKS Hamiltonian and overlap matrices, respectively, with the elements:

$$H_{\mu\mu'}(\mathbf{k}) = \sum_{\mathbf{R}} e^{i\mathbf{k} \cdot \mathbf{R}} \int_{\mathbb{R}^3} \chi_\mu^\dagger(\mathbf{r}) \hat{H} \chi_{\mu'}(\mathbf{r} - \mathbf{R}) d^3\mathbf{r}, \quad (4a)$$

$$S_{\mu\mu'}(\mathbf{k}) = \sum_{\mathbf{R}} e^{i\mathbf{k} \cdot \mathbf{R}} \int_{\mathbb{R}^3} \chi_\mu^\dagger(\mathbf{r}) \chi_{\mu'}(\mathbf{r} - \mathbf{R}) d^3\mathbf{r}. \quad (4b)$$

Due to the dependence of  $H(\mathbf{k})$  on the electron density and its gradient that are determined from  $c(\mathbf{k})$ , Eq. (3) must be solved self-consistently, though the SOC terms are often neglected in the self-consistent procedure and only included a posteriori as a perturbation to save computational time [71]. Techniques that employ various choices for the basis functions  $\chi_\mu$ , such as numerical [72–74], Slater-type [75, 76], or Gaussian-type basis sets [54, 77], have been developed for periodic systems at various relativistic levels of the theory.

The method presented in this work is based on Gaussian-type orbitals (GTOs) commonly used in quantum chemistry for calculations of properties, electronic structures, and electron correlations in molecules. The use of GTOs for solids offers several advantages. For instance, a unified representation of wave functions in a variety of systems (molecules, polymers, 2D materials,

crystals) allows for building on existing quantum chemistry approaches, such as the accurate treatment of correlation [78–81], reduced cost of evaluating the exact exchange [82], and efficient algorithms that scale linearly with system size [83, 84]. In 2D materials that are only a few atomic layers thick, Bloch functions are straightforwardly constructed to satisfy the Bloch theorem only across the two periodic dimensions by explicitly restricting  $\mathbf{R}$  and  $\mathbf{k}$  in Eq. (2) to 2D lattice vectors. As a consequence, the system is not artificially replicated in the nonperiodic dimension. For comparison with calculations employing plane waves, this situation would correspond to the limit of infinitely large vacuum layers (or zero hopping) between the replicated images. Finally, explicit self-consistent treatment of SOC for all electronic states on an equal footing without adopting the muffin-tin or pseudopotential approximations provides access for studies of x-ray absorption spectroscopy [85] and magnetic response properties associated with nuclear spins [86, 87].

Modelling solid-state systems with GTOs in the non-relativistic framework was pioneered by Pisani and Dovesi [88–90], later joined by several other groups [83, 84, 91]. However, standard GTO basis sets are constructed by optimizing calculations on atoms and thus contain basis functions with small exponents to describe the asymptotic behavior of the atomic wave functions. These diffuse functions severely hamper the application of GTOs to solids and cause numerical instabilities [83, 92–94]. The numerical issues can be circumvented by removing the most diffuse basis functions at the onset of the calculation [95–97] or by constructing system-specific basis sets using reoptimized Gaussian exponents and contraction coefficients [93, 98]. The former strategy risks producing low quality results [54, 99] whereas the latter strategy sacrifices the transferability of the so-constructed basis sets and requires availability of advanced code features (basis set optimization). Pre-optimized all-electron basis sets are also not available for heavy elements [93]. The importance of numerical stability is even more pronounced in relativistic theories where the additional wave-function components increase the variational freedom, and the restricted kinetic balance (RKB) condition [100] must be satisfied to prevent the collapse of the spectral gap between the positive- and negative-energy states.

In this paper, we demonstrate that accurate and converged results can be obtained for 2D TMD monolayers in various structural phases using commonly available all-electron valence triple- $\zeta$  basis sets in the fully relativistic framework without the need of modifying or reoptimizing the basis functions. Our approach builds on the quaternion algebra-based theory [54] implemented here with careful numerical considerations to ensure robustness of the implementation and the resolution-of-the-identity (RI) approximation for the Coulomb four-center integrals [101–103] that reduces the computational cost of otherwise time-consuming calculations by more than three orders of magnitude. We show how the canonical

orthogonalization can be used to construct numerically well-behaved orthonormal bases in momentum space in the 4c setting and derive a criterion for assessing the quality of the RKB condition in such bases. We discuss a parallel algorithm for the electronic structure solver exhibiting minimal input/output (IO) disk communication and memory overhead that is applicable to unit cells with several thousand basis functions and thousands of  $\mathbf{k}$  points. The method presented here is implemented in the RESPECT code [55] and used to calculate the band structures of the hexagonal (2H), tetragonal (1T), and distorted tetragonal (1T') phases of selected TMDs. For the 1T' phase, we evaluate the  $\mathbb{Z}_2$  invariant within our real-space GTO-based scheme and confirm the findings of Qian [11] that the 1T' phase of  $\text{MX}_2$  is topologically nontrivial.

## II. RESULTS AND DISCUSSION

We calculated the electronic band structures of six TMDs ( $\text{MoS}_2$ ,  $\text{MoSe}_2$ ,  $\text{MoTe}_2$ ,  $\text{WS}_2$ ,  $\text{WSe}_2$ ,  $\text{WTe}_2$ ) in the 2H, 1T, and 1T' structural phases using our 4c all-electron GTO method. We compared our 2H and 1T results with the band structures presented in Ref. 6 obtained from the method of Te Velde and Baerends [104]. For the 1T' phase, we used the VASP program package [105] to investigate how our all-electron method performs compared to the pseudopotential approximation. Due to the presence of heavy atoms, all these TMDs exhibit significant scalar relativistic and SOC effects. We investigated three different levels of theory: nonrelativistic (nr) theory with the infinite speed of light, Dirac-based 4c scalar relativistic (sr) theory without SOC, and Dirac-based 4c fully relativistic (fr) theory with SOC included. For all calculations reported in this work, we employed the nonrelativistic GGA-type XC functional PBE [106]. For the 4c calculations, the Gaussian finite nucleus model of Visscher and Dylla [107] was used instead of point nuclei in order to regularize the singularity of the lower components of the wave function evaluated at the atomic centers. All electronic structure optimizations were performed using the relaxed unit cell geometries taken from Ref. 6 (2H and 1T phases) and Ref. 11 (1T' phase). For the momentum-space Brillouin zone integration, we used the  $\Gamma$ -centered mesh of  $\mathbf{k}$  points of  $11 \times 11$  for the 2H and 1T' phases and  $33 \times 33$  for the metallic 1T phase. When comparing band structures  $\varepsilon_n^{(1)}(\mathbf{k})$  and  $\varepsilon_n^{(2)}(\mathbf{k})$  obtained using two different methods or computational settings, we evaluate the maximum difference between the energy eigenvalues as well as the root-mean-square deviation (“band delta”) [71]

$$\Delta_b(\mathcal{W}) = \sqrt{\frac{1}{N_E} \sum_{\substack{\mathbf{k}, n \\ \varepsilon_n^{(1)}(\mathbf{k}) \in \mathcal{W} \\ \varepsilon_n^{(2)}(\mathbf{k}) \in \mathcal{W}}} \left( \varepsilon_n^{(1)}(\mathbf{k}) - \varepsilon_n^{(2)}(\mathbf{k}) \right)^2}, \quad (5)$$

where  $\mathcal{W} = [\varepsilon_l, \varepsilon_u]$  is an energy window chosen for comparison, the summations run over all energy states along a path of  $\mathbf{k}$  points for which both  $\varepsilon_n^{(1)}(\mathbf{k})$  and  $\varepsilon_n^{(2)}(\mathbf{k})$  lie inside the window  $\mathcal{W}$ , and  $N_E$  is the total number of such states.

### A. Numerical and basis-set accuracy

Numerical instability in simulations involving periodic systems with GTOs originate from two distinct, albeit related, reasons [83, 92]. First, the numerical accuracy of the KS Hamiltonian matrix can be insufficient when various approximations necessary for solid-state simulations are introduced for basis sets with diffuse functions. Diffuse basis functions can extend over a very large number of unit cells, and the overlap between two such functions exhibits a much slower decay than their more localized counterparts. If these overlaps are neglected too soon, the summations in Eqs. (4) are not converged, causing the overlap matrix  $S_{\mu\mu'}(\mathbf{k})$  to be indefinite, *i.e.* having negative eigenvalues. This problem can be mitigated by including a large number of basis function products  $\chi_\mu^\dagger(\mathbf{r})\chi_{\mu'}(\mathbf{r} - \mathbf{R})$ , which in turn increases the memory requirements for storage of matrices. To this end, in the periodic module of RESPECT, we implemented sparse data structures in real space in combination with quaternion algebra to efficiently handle spin-orbit-coupled wave-function components. Such a versatile approach allows us to retain the accuracy necessary for numerical robustness with a very small additional memory footprint.

The second problem is associated with overcompleteness (linear dependencies) of the basis that causes matrices in Eq. (3) to be ill-conditioned and introduces errors and instabilities in matrix operations such as diagonalization. This occurs when the eigenvalues of the momentum-space overlap matrix drop below  $10^{-7}$ , which is often the case for larger basis sets (such as TZ). For instance, the smallest eigenvalue of the overlap matrix of  $\text{WTe}_2$  in the 1T' phase is  $10^{-11}$ , while the remaining eigenvalues span over 12 orders of magnitude. Subsequently, very large elements  $\sim 10^8$  are accumulated in the density matrix, which prohibits the successful completion of the ground-state convergence procedure. To avoid such errors, we construct an orthonormal basis so that the redundant basis functions are projected out. However, we found that truncating the space spanned by orthonormal basis functions used for describing the lower wave-function components lead to the formation of artificial states inside the band gap for some  $\mathbf{k}$  points of the band structure. This can be understood by realizing that the RKB condition is violated by the truncation process. In order to numerically control how much of the RKB is lost, we derived the matrix form of the RKB condition in a general basis and the expression for the truncation error. More details on the process of constructing the orthonormal basis in the 4c framework is described in the

Methods Sec. IV A.

For all atoms, we employed the relativistic triple- $\zeta$  (TZ) basis sets developed by Dyall for d elements [108–110] and for p elements [111, 112]. The basis sets used were uncontracted and contained high-angular momentum correlating functions for several outer shells and functions for dipole polarization of the valence shells. Our initial tests using the smaller double- $\zeta$  (DZ) basis from the same family yielded results with inconsistent quality across  $\mathbf{k}$  points – for instance, the band energy at the  $M$  point of 2H  $\text{MoS}_2$  was improved by 20 meV when the TZ basis was used, while for other  $\mathbf{k}$  points, this difference was only about 6 meV. Similarly, the differences in the band structures of 2H  $\text{WS}_2$  (including the band gap) between the DZ and TZ basis sets were 20-30 meV. Hence, to ensure that our results are well-converged for all  $\mathbf{k}$  points and that the target accuracy is sufficient for reliable comparisons with other methods, we chose the TZ basis in all calculations reported here.

The basis sets employed contained very diffuse functions with several exponents  $< 10^{-2}$  a.u. The extent of the most diffuse function on Mo and W was 18.2 Å and 17.2 Å, respectively, causing the basis function to span more than a hundred unit cells of the 2D film. This in turn results in several hundred thousand charge distributions interacting with themselves and their periodic replicas when the four-center Coulomb integrals are evaluated. Such calculations are currently unfeasible on common supercomputers as they can consume a notable portion of allocated resources. However, within the RI approximation, the charge distributions only interact with the electron density that is expanded using an atom-centered auxiliary basis. Since the number of the three-center terms needed is smaller than the number of four-center terms typically by three orders of magnitude, the evaluation of the Coulomb operator becomes affordable. Tests that we performed on various systems including selected 2H and 1T' structures studied here in both the nr and fr settings indicate that the maximum error introduced by the RI approximation is very small – only a few tens of  $\mu\text{eV}$ .

Our implementation allowed us to explore the validity of removing diffuse functions from the GTO basis sets before starting the electronic-structure optimization — an approach that is commonly employed for the sake of accelerating and numerically stabilizing calculations of periodic systems using GTOs [95–97]. From the TZ basis sets, we deleted all exponents  $< 0.1$  which for most atoms meant removing one to two functions in each of the s, p, d, and f shells. Even though this modification reduced the computational cost by a factor between five and six in case of the nr theory and a factor of four in case of the 4c theory, we observed lowered accuracy of the eigenenergies of some bands and  $\mathbf{k}$  points. For instance, the difference between the energy of the  $\Gamma$  point of the valence band of 2H  $\text{WTe}_2$  obtained from the calculation using the truncated and full basis sets was 0.1 eV. The virtual bands located 2.5 eV above the Fermi level

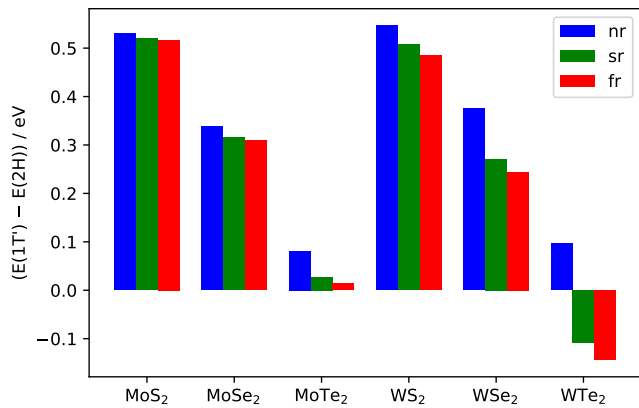


FIG. 1. Relative total energy of the 1T' phase of TMD monolayers per MX<sub>2</sub> calculated with respect to the 2H phase. The results were obtained for nr, sr, and fr Hamiltonians and show the relativistic effects on the structural stability.

were, in general, poorly described with the truncated basis set. Hence, our results indicate that removing the diffuse functions on the onset of the calculation is neither justified nor necessary.

### B. Stability of phases

Before inspecting individual structural phases and validating our approach, we compare the total energies of each phase. Our results confirm the findings of Qian *et al.* [11] — for all systems except WTe<sub>2</sub>, the 2H phase was found to be the ground-state structure with the lowest energy, followed by the higher-energy 1T' phase. The metallic 1T phase is thermodynamically unstable and the systems undergo Jahn–Teller distortion, relaxing to the 1T' phase [11]. In the case of WTe<sub>2</sub>, the energy of the 1T' phase is below the 2H phase, which makes the 1T' phase the most stable.

Our study allows for a uniform treatment of relativistic effects for all atoms and all electrons, as opposed to calculations employing pseudopotentials, which offer less control over how relativity is handled for light and heavy elements. We found that it is the inclusion of the scalar relativistic effects that decreases the energy of the 1T' phase with respect to the 2H phase. Including the SOC further lowers the energy of the 1T' phase. For the heaviest system, WTe<sub>2</sub>, this energy lowering becomes sufficient to change the ground-state phase from 2H to 1T'. Fig. 1 summarizes our results for all systems at the nr, sr, and fr levels of theory and shows the relative energy differences between the 1T' and 2H phases. Hence, without relativity, the ground-state structure of all six systems would be 2H.

TABLE I. Band gaps and SOC-induced (Rashba) splitting of the valence band at the K point of TMD monolayers in the 2H phase calculated for nr, sr, and fr Hamiltonian. The values in the round and square brackets are taken from Refs. 6 and 113, respectively.

	Band gap ( $E_g$ , eV)			Rashba splitting (eV)
	nr	sr	fr	fr
MoS <sub>2</sub>	1.820	1.812 (1.82)	1.734 (1.74)	0.146 [0.147]
MoSe <sub>2</sub>	1.560	1.550 (1.56)	1.442 (1.45)	0.185 [0.186]
MoTe <sub>2</sub>	1.171	1.154 (1.15)	1.018 (1.01)	0.218
WS <sub>2</sub>	2.060	1.984 (1.98)	1.628 (1.64)	0.416 [0.433]
WSe <sub>2</sub>	1.741	1.630 (1.63)	1.300 (1.33)	0.460 [0.463]
WTe <sub>2</sub>	1.332	1.194 (1.18)	0.863 (0.87)	0.479

### C. 2H and 1T phases

The 2H and 1T phases of the TMDs both contain three atoms (one metal and two chalcogenides) in the primitive unit cell. However, the structural differences between these two phases lead to their distinct electronic properties. Whereas the 1T phase is space-inversion-symmetric with a metallic electronic structure, the 2H systems are semiconductors with broken space inversion. In combination with the strong SOC, this broken inversion symmetry leads to “giant” spin–orbit-induced Rashba splittings in 2H MX<sub>2</sub> [29].

To validate the approach presented in this work, we calculated the band structures at the nr, sr, and fr levels of theory using all-electron bases. The resulting band diagrams traversing high-symmetry  $\mathbf{k}$  points obtained with and without SOC can be found in Figs. S1 (2H) and S2 (1T) in the supplementary material (SM). The nonrelativistic results differ significantly from those obtained from the relativistic theories and are not shown. For the 2H and 1T phases, sr band structures are available in the 2D materials' Atlas of Miró, Audiffred, and Heine [6] that we used for comparison. We conclude that our results agree very well at the sr level with the Atlas results.

In the MoTe<sub>2</sub> and WTe<sub>2</sub> band structures of the 1T phase shown in Fig. S2, it is possible to see very small SOC-induced “Rashba-like” spin splittings of the order of tens of meV. However, such splittings should not be present for the inversion-symmetric 1T phase, and all the bands should be strictly doubly degenerate. We found that this observation can be attributed to small deviations (about 0.04 Å) in the unit cell geometry of MoTe<sub>2</sub> and WTe<sub>2</sub> from the tetragonal lattice, that is, the 1T structure used does not exhibit exact inversion symmetry. The geometries of the other systems do not show any deviations from 1T, and we observed exact double degeneracy of bands. Finally, we note that including the

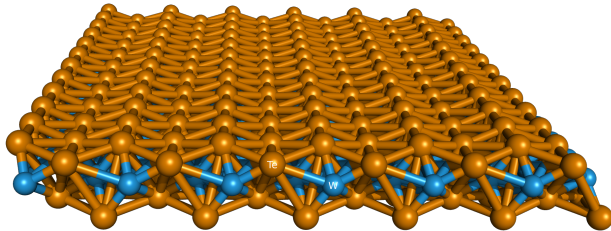


FIG. 2. The structure of the 1T' phase of monolayer TMDs.

SOC in the computational framework lifted the degeneracy occurring at intersection points of the overlapping valence and conduction bands of the metallic 1T phase. The values of the SOC-induced vertical gaps at the K point are reported in Table SI of the SM.

Table I contains the values of the nr, sr, and fr band gaps of the 2H phase, as well as the Rashba splittings of the valence band at the K point. The small discrepancies between the results obtained with the method presented here and the Atlas approach we attribute to differences in the chosen methodologies. In the Atlas work, the relativistic effects are treated with the zeroth-order regular approximation (ZORA) [114], which is a 2c technique that requires numerical integration schemes due to the appearance of the potential in the denominator of the Hamiltonian. In contrast, the Hamiltonian used here is 4c with most of the integrals evaluated analytically. The basis sets employed should not cause any significant deviations, since both sets of calculations were carried out with TZ quality bases with several polarization functions. Finally, we note that the Atlas results included empirical D3 treatment of London dispersion interactions [115] that we did not consider in this work. The WSe<sub>2</sub> material, for which we observed the largest difference of 30 meV in the fr setting, we furthermore benchmarked against a calculation with the bigger quadruple- $\zeta$  (QZ) basis set. The band energies improved only marginally, *i.e.* by units of meV. Hence, we believe that our band structures are well converged with respect to the basis set as well as the relativistic Hamiltonian and should serve as the reference results for these systems for the PBE functional.

#### D. 1T' phase

The 1T' phase of MX<sub>2</sub> is formed from the 1T structure by a spontaneous lattice distortion in which the unit cell period is doubled along one in-plane direction, which creates zigzag chains along the perpendicular in-plane direction [117]. The TMDs were shown to host the QSH effect in the 1T' structure, *i.e.* the existence of time-reversal-symmetry protected edge states that enable conduction of electrical currents on the surface of the material [11]. From a computational viewpoint, the

TABLE II. Root-mean-square deviation between the band structures of TMD monolayers obtained from the RESPECT and VASP codes at the fr level of theory (including SOC) using Eq. (5). The valence region  $\mathcal{W}_{\text{val}}$  ranges from  $-10$  eV to  $0$  eV (shifted to the Fermi level) and the conduction region  $\mathcal{W}_{\text{con}}$  ranges from  $0$  eV to  $5$  eV.

	Band delta (meV)					
	MoS <sub>2</sub>	MoSe <sub>2</sub>	MoTe <sub>2</sub>	WS <sub>2</sub>	WSe <sub>2</sub>	WTe <sub>2</sub>
$\Delta_{\text{b}}(\mathcal{W}_{\text{val}})$	12.0	8.4	11.7	34.6	25.6	20.2
$\Delta_{\text{b}}(\mathcal{W}_{\text{con}})$	40.5	28.4	32.8	26.2	23.4	42.0

1T' phase has not been studied in the literature to the same extent as the 2H and 1T counterparts. Here, we calculated the electronic band structures of the 1T' MX<sub>2</sub> using the all-electron 4c method presented in this work as well as the pseudopotential method as implemented in the VASP program package [105]. For the VASP calculations, we used an energy cutoff of 500 eV and the Brillouin zone  $\mathbf{k}$ -point sampling of  $11 \times 15 \times 1$ . We also tested a denser mesh of  $\mathbf{k}$  points without observing any notable differences. To avoid artificial interactions between the periodic images of the MX<sub>2</sub> layers that appear when 2D systems are studied using plane waves with the periodic boundary conditions, a vacuum region of 20 Å was applied in the direction perpendicular to the 2D film.

The band structures obtained from the RESPECT and VASP codes with SOC are presented in Fig. 3. The values of the band delta differences between the two codes are shown in Table II, evaluated separately for the occupied (valence) and virtual (conduction) energy regions. In general, the differences are of the order of tens of meV and are larger in the virtual region. The biggest discrepancies close to the Fermi level are seen in WS<sub>2</sub>, while the overall largest band delta values are found in MoS<sub>2</sub> and WTe<sub>2</sub>. For comparison, we performed tests of the numerical convergence of the GTO method by tuning various parameters of the RESPECT code. In particular, we modified the number of removed momentum-space basis functions in the orthonormal basis (see Sec. IV A), tightened the lattice-sum convergence thresholds, as well as turned off the RI approximation of the Coulomb integrals. Such modifications had a negligible effect on our GTO results; the band delta values between the higher accuracy calculations and the results shown here reached tens of  $\mu\text{eV}$ . Bigger differences were observed only when we benchmarked the WS<sub>2</sub> TZ calculation against the QZ basis set. Still, the energies of the bands close to the Fermi level changed by 1–6 meV, and the values of the band deltas for the intervals  $-10$  eV to  $0$  eV and  $0$  eV to  $5$  eV were  $\Delta_{\text{b}}(\mathcal{W}_{\text{val}}) \approx 4$  meV and  $\Delta_{\text{b}}(\mathcal{W}_{\text{con}}) \approx 10$  meV, respectively. To conclude, despite that minor improvements to the band structure are possible when larger basis sets are employed in the calculations, our TZ results can be considered as the reference for benchmarking performance of other approximate methods, for instance, for studying accuracy of various pseudopotentials.

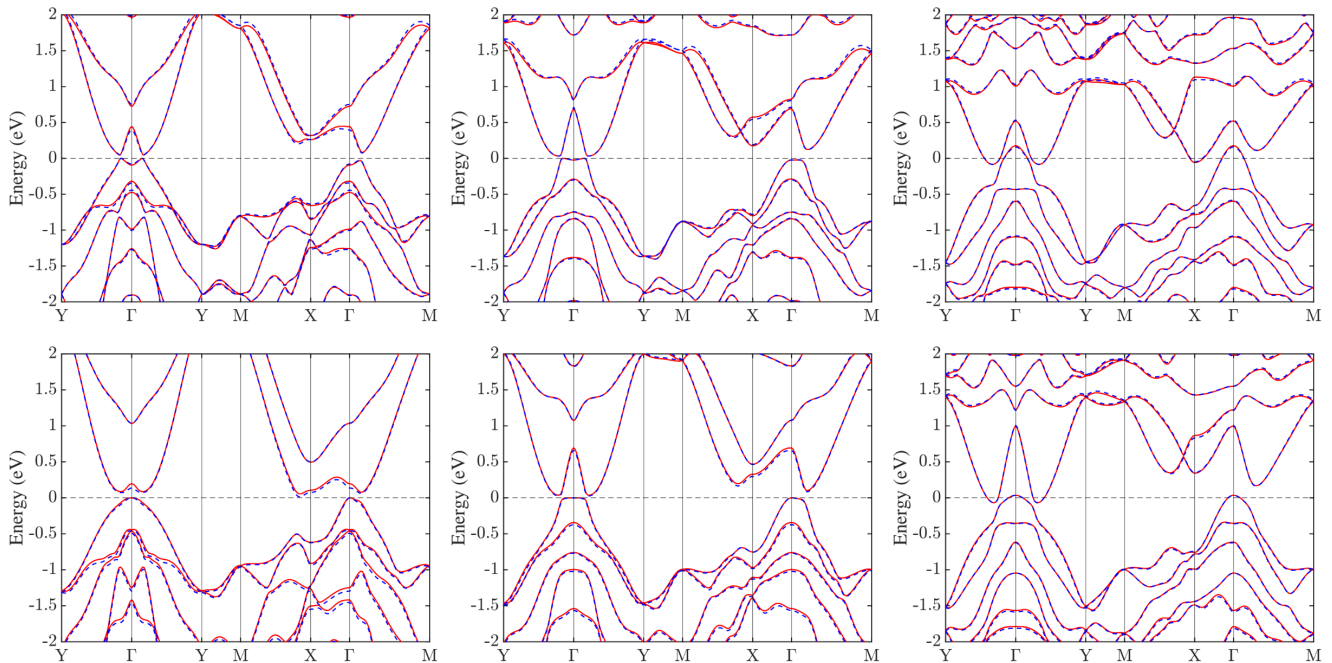


FIG. 3. Comparison of band structures of  $\text{MX}_2$  monolayers in the  $1\text{T}'$  phase obtained from the RESPECT (dashed lines) and VASP (full lines) codes at the relativistic level of theory including SOC. From the top left to bottom right:  $\text{MoS}_2$ ,  $\text{MoSe}_2$ ,  $\text{MoTe}_2$ ,  $\text{WS}_2$ ,  $\text{WSe}_2$ ,  $\text{WTe}_2$ . The horizontal dashed black line marks the Fermi level. The path traversing high-symmetry  $\mathbf{k}$ -points in the reciprocal-space unit cell was chosen according to Ref. 116.

We explored the topological nature of the  $1\text{T}'$  phase of the  $\text{MX}_2$  systems by first verifying that the band-gap opening is due to the SOC. Fig. S3 in the SM shows that energy degeneracies occurring at points where the valence band crosses the conduction band are lifted when SOC is included in the description. A band gap is opened for all systems except  $\text{MoTe}_2$  and  $\text{WTe}_2$  that remain metallic despite the band inversion. The lattice distortion in the  $1\text{T}'$  phase of the 2D TMDs does not break the inversion symmetry. Hence, we used the parity of the Bloch states evaluated at the time-reversal invariant momenta (TRIM) to calculate the  $\mathbb{Z}_2$  invariant [118]. Our results for the parities of the individual Kramers pairs agree with those obtained by Qian [11], which yields  $(-1)^\nu = 1$  for all six TMDs and confirms the existence of the surface edge states hallmarking the quantum spin Hall phase.

### III. CONCLUSION AND OUTLOOK

2D TMDs rank among the materials attracting highest interest for hosting exotic phenomena that promise applications in spintronic devices and quantum computing. Theoretical predictions and understanding of such applications relies on accurate description of relativistic effects in the heavy atoms that are main constituents of these materials. To enable studies of materials that are strongly influenced by relativistic effects and electron wave functions close to nuclei and offer a uniform

theoretical framework for solids and molecules where all electronic states are described on an equal footing, we have presented an approach here that builds on the most widely used basis sets in quantum chemistry.

GTOs provide a convenient link between finite and periodic or extended systems, yet their use for solids has been met with many technical difficulties that sparked scepticism in the community; it was even suggested that GTOs should be avoided altogether for condensed matter calculations [99]. However, in this work, we show how the common limitations associated with GTOs can be overcome, and we demonstrated that the convergence with respect to the basis set limit is possible even in the fully relativistic 4c setting. To mitigate numerical and performance issues, our method is based on the quaternion algebra, linear-scaling data structures, RI approximation of the Coulomb integrals, orthonormal momentum-space bases that sufficiently preserve the RKB condition, and a parallel electronic structure solver with minimal required IO operations. Our in-depth analysis of the 2H,  $1\text{T}$ , and  $1\text{T}'$  phases of 2D TMDs indicates that our all-electron 4c results can serve as the reference for developing pseudopotentials or approximate 2c relativistic techniques. Finally, we confirmed the existence of the quantum spin Hall effect in the  $1\text{T}'$  phase of  $\text{MX}_2$  by calculating the  $\mathbb{Z}_2$  invariant within our real-space formulation, and we attributed the origin of the lower ground-state energy of  $\text{WTe}_2$  in the  $1\text{T}'$  phase than  $2\text{H}$  phase to the (scalar) relativistic effects.

The work here is important for opening a pathway for further developments that leverage quantum chemistry methods for studying properties strongly affected by the relativity and SOC without sacrificing the possibility to directly model the core region of the electron charge and spin densities. For instance, accurate relativistic first-principles calculations of the spin Hamiltonian parameters (*e.g.* hyperfine coupling constants, Zeeman interactions, or zero-field splitting) are needed for determining spin dynamical properties of spin defects in semiconductors [62] to help us find suitable materials hosting qubits. Our all-electron method can also be used for generation of new accurate pseudopotentials, particularly for the systems containing heavy elements in high oxidation states.

#### IV. METHODS

##### A. Construction of orthonormal momentum-space basis

Throughout this section, we assume Einstein's implicit summation over doubly repeating indices.

In order to avoid variational collapse associated with an incomplete basis representation of the lower components of the wave function [119] and to obtain the correct nonrelativistic limit of the kinetic energy operator in a finite basis, we impose the RKB condition [100] for the basis bispinors  $\chi_\mu(\mathbf{r})$  in real space. Hence, we require that [43, 49, 53, 55, 120, 121]

$$\chi_\mu(\mathbf{r}) \equiv \begin{pmatrix} \mathbb{I}_2 & 0_2 \\ 0_2 & \frac{1}{2c}\boldsymbol{\sigma} \cdot \mathbf{p} \end{pmatrix} g_\mu(\mathbf{r} - \mathbf{A}_\mu), \quad (6)$$

where  $\mathbb{I}_2$  is the  $2 \times 2$  identity matrix,  $\mathbf{p} \equiv -i\nabla$  is the electron momentum operator, and  $g_\mu$  are scalar basis functions centered on atom positions  $\mathbf{A}_\mu$ . Due to the multicomponent structure of  $\hat{H}$  and  $\chi_\mu$ ,  $H_{\mu\mu'}$  and  $S_{\mu\mu'}$  in Eq. (4) are  $4 \times 4$  complex matrices for each pair  $\mu, \mu'$  and for each  $\mathbf{k}$ . For the functions  $g_\mu$ , we choose the primitive spherical Gaussian-type orbitals (GTOs)

$$g_\mu(\mathbf{r}) \equiv \mathcal{N} Y_{lm}(\vartheta, \varphi) e^{-\alpha r^2}, \quad (7)$$

where  $\mathcal{N}$  is the normalization constant,  $\alpha$  is the Gaussian exponent, and  $Y_{lm}(\vartheta, \varphi)$  are the spherical harmonics. The GTO basis is commonly implemented in many quantum chemistry codes [90, 91, 122–126]. For computational reasons, integrals in Eqs. (4) are evaluated analytically by solving recurrence relations [127] formulated in terms of the Cartesian GTOs [128]. The resulting integrals are then transformed to spherical GTOs.

To construct an orthonormal basis in momentum space, let us first define a nonorthogonal basis from  $\chi_{\mu\mathbf{R}}(\mathbf{r}) \equiv \chi_\mu(\mathbf{r} - \mathbf{R})$  as

$$\chi_\mu(\mathbf{k}) = \frac{1}{\sqrt{|\mathcal{K}|}} \sum_{\mathbf{R}} e^{i\mathbf{k} \cdot \mathbf{R}} \chi_{\mu\mathbf{R}}. \quad (8)$$

A new basis is obtained using the transformation

$$\varphi_p(\mathbf{k}) = \chi_\mu(\mathbf{k}) B_p^\mu(\mathbf{k}). \quad (9)$$

From here, we for clarity drop the dependence of all matrices on  $\mathbf{k}$ . The matrix  $B$  can be chosen so that  $\varphi_p$  are orthonormal, *i.e.*  $B^\dagger S B = \mathbb{I}$ . We perform the canonical orthogonalization

$$B = U s^{-1/2} \Lambda, \quad (10)$$

where  $U$  is the unitary matrix of eigenvectors and  $s$  is the diagonal matrix of eigenvalues, both obtained from diagonalizing the overlap matrix  $S$ .  $\Lambda$  is a rectangular matrix consisting of the square identity matrix and zero rows that correspond to the basis functions that are projected out. In case no projections are required,  $\Lambda$  is simply the identity matrix.

In the relativistic 4c theory,  $\chi_\mu$  take the bispinor form of Eq. (6), and the  $B_p^\mu$  become  $4 \times 4$  matrices for each  $\mu, p$ . However, let us now consider a general basis set of bispinors  $\chi_\mu$  with  $\chi_\mu^L$  and  $\chi_\mu^S$  denoting the  $2 \times 2$  large (upper) and small (lower) components of the basis, respectively. Similarly, let  $\varphi_p^L \equiv \chi_\mu^L X_p^\mu$  and  $\varphi_p^S \equiv \chi_\mu^S Y_p^\mu$  denote the transformed (*e.g.* orthonormalized) large and small components of the basis, respectively,  $X$  and  $Y$  forming a block-diagonal matrix  $B$  in Eq. (9). The DKS Hamiltonian takes the matrix form

$$H = \begin{pmatrix} V_{LL} & c\Pi_{LS} \\ c\Pi_{SL} & V_{SS} - 2c^2 S_{SS} \end{pmatrix}, \quad (11)$$

where  $V_{LL}, V_{SS}, \Pi_{LS}, \Pi_{SL}$  are the matrix representations of their respective operators in the  $\chi_\mu$  basis, and  $S_{SS}$  is the overlap matrix for the small-component basis. Ensuring numerical stability requires projecting out basis functions  $\varphi_p^L$  and  $\varphi_p^S$  corresponding to the smallest eigenvalues of the 4c overlap matrix. At the same time, removing  $\varphi_p^S$  functions degrades the RKB condition that is no longer satisfied exactly in the new basis, which can lead to the emergence of artificial in-gap states. Here, we proceed by showing how we numerically track this basis truncation error. First, we express the RKB condition in the matrix form using the arbitrary basis  $\chi_\mu$ . If we write the 4c eigenvalue problem with the Hamiltonian matrix in Eq. (11) and eliminate the small-component wave-function coefficients, we obtain

$$\left[ V_{LL} + \frac{1}{2} \Pi_{LS} \mathcal{B}_{SS}^{-1}(\varepsilon) \Pi_{SL} \right] c_L = \varepsilon S_{LL} c_L, \quad (12)$$

where

$$\mathcal{B}_{SS}(\varepsilon) = S_{SS} + \frac{\varepsilon S_{SS} - V_{SS}}{2c^2}, \quad (13)$$

$c_L$  are the coefficients of the large component of the wave function, and  $\varepsilon$  is the one-electron energy. Imposing the requirement that the nonrelativistic Hamiltonian is recovered in the limit  $c \rightarrow \infty$  gives the following condition

$$T_{LL} = \frac{1}{2} \Pi_{LS} S_{SS}^{-1} \Pi_{SL}, \quad (14)$$

where  $T_{LL}$  is the nonrelativistic kinetic energy matrix in the basis of the large component. We note, that the choice of bispinors  $\chi_\mu$  as in Eq. (6) satisfies Eq. (14) analytically, since  $\Pi_{LS} = \Pi_{SL} = \frac{1}{c}T_{LL}$  and  $S_{SS} = \frac{1}{2c^2}T_{LL}$ . In the transformed basis  $\varphi_p$ , Eq. (14) reads

$$X^\dagger T_{LL} X = \frac{1}{2} X^\dagger \Pi_{LS} Y (Y^\dagger S_{SS} Y)^{-1} Y^\dagger \Pi_{SL} X. \quad (15)$$

This RKB condition remains valid as long as two conditions are met: The former basis  $\chi_\mu$  satisfies Eq. (14), and the inverse  $Y^{-1}$  exists, *i.e.* the new basis spans the same space as the former one. By requiring that the new basis is orthonormal ( $Y^\dagger S_{SS} Y = \mathbb{I}$ ), this condition simplifies to

$$X^\dagger T_{LL} X = \frac{1}{2} X^\dagger \Pi_{LS} Y Y^\dagger \Pi_{SL} X, \quad (16)$$

and the existence of  $Y^{-1}$  implies that  $S_{SS}^{-1} = Y Y^\dagger$ . However, orthonormalization procedures that involve removing eigenvectors in the orthonormal basis of  $\varphi_p^S$  by using a rectangular  $\Lambda$  in Eq. (10) do not generally preserve the RKB condition. Hence, in the 4c framework, improving the conditioning of matrices by projecting out redundant basis functions can sacrifice the RKB between the  $L$  and  $S$  components.

In order to assess the quality of the orthonormal basis for the lower components of the wave function, we calculate how much of the RKB condition is lost by the transformation to the reduced orthonormal basis. To this end, we evaluate

$$e = \max \left[ X^\dagger \left( \frac{1}{2c^2} T_{LL} Y Y^\dagger T_{LL} - T_{LL} \right) X \right], \quad (17)$$

for each  $\mathbf{k}$ . Here,  $\max$  indicates the largest matrix element. We found, that large values of  $e$  ( $> 10^{-5}$ ) could be associated with the emergence of artificial states in the band structure. To keep the error in the RKB small, for every  $\varphi_p^S$  function that is projected out, we also remove the corresponding  $\varphi_p^L$  function regardless of how large the eigenvalue of the overlap matrix  $S_{LL}$  is for this function. This means that the  $\varphi_p^L$  must be removed even if it is not causing overcompleteness of the large-component subspace. We note, that these measures were necessary for moderately-sized (triple- $\zeta$  and quadruple- $\zeta$ ) basis sets, but the numerical issues were not observed in case the smaller double- $\zeta$  basis was used. Finally, the process of orthonormalization and removal of redundant functions heavily depends on  $\mathbf{k}$ , so the implementation of the electronic structure solver must have the flexibility to account for matrices with different sizes for each  $\mathbf{k}$ .

## B. Parallel electronic structure solver

Construction of the ground-state one-electron wave functions within the self-consistent field (SCF) theory consists of two distinct steps that are iterated repeatedly

until self-consistency is reached. The DKS Hamiltonian and overlap matrices in Eqs. (4) are first assembled in real space using the GTO basis. These are then transformed to reciprocal space, and Eq. (3) is solved in the orthonormal basis using matrix algebra (multiplications and diagonalizations). Large-scale or high-throughput calculations of band structures of solids require efficient algorithms that offer good (ideally linear) scaling with respect to the number of computer cores used as well as the size of the unit cell. This must be accomplished for both of the SCF solver steps. The demand for efficiency is especially important for all-electron 4c calculations, where the matrix sizes are much larger and even otherwise negligible matrix operations become time-consuming.

The evaluation of the DKS Hamiltonian matrix elements is dominated by the electron–electron Coulomb contributions for DFT simulations with pure exchange–correlation functionals. We adopt the resolution-of-the-identity (RI) approach [101–103] (also known as the density fitting procedure) combined with multipole expansions [84, 129] to significantly reduce the overall cost of the Coulomb terms. The RI method approximates the electron density by a linear combination of auxiliary basis functions centered on atoms, as opposed to the exact treatment of the four-center Coulomb integrals where the orbital products that constitute the density are expanded individually. Our RI implementation differs from that of previous authors [84, 130], and the theoretical challenges associated with the divergent terms in the Coulomb metric matrix of periodic systems together with details of this RI method are going to be presented elsewhere.

Once the real-space matrix elements are calculated, the remaining steps – transformation to reciprocal space, orthonormalization procedure, matrix diagonalization – is performed independently for each  $\mathbf{k}$ . We exploit the factorization of the reciprocal-space tasks by employing message-passing-interface (MPI) directives which allow high level of parallelization to be achieved due to almost no communication needed among various MPI processes. Each process utilizes multiple OpenMP threads when calling internally parallelized matrix libraries. However, in order to construct the electron density

$$\rho(\mathbf{r}) = \sum_n \int_{\mathcal{K}} f_n(\mathbf{k}) \psi_n^\dagger(\mathbf{k}; \mathbf{r}) \psi_n(\mathbf{k}; \mathbf{r}) d^3\mathbf{k}, \quad (18)$$

where  $f_n(\mathbf{k})$  is the occupation number of the  $n$ -th band and  $\psi_n(\mathbf{k}; \mathbf{r})$  are the Bloch functions defined in Eq. (2), the band energies  $\varepsilon_n(\mathbf{k})$ , from which the occupations are determined, must be known for all  $\mathbf{k}$ . Hence, the evaluation of the electron density (needed for subsequent SCF iterations) occurs after all the wave-function coefficients  $c_n^\mu(\mathbf{k})$  and energies are found. In the all-electron 4c framework, the coefficient matrices are too large to be stored in memory for all  $\mathbf{k}$ , and storing the matrices on disk hampers the MPI parallelization due to significantly increased I/O communication. To this end, we partition

the electron density into two terms

$$\rho(\mathbf{r}) = \rho_c(\mathbf{r}) + \rho_v(\mathbf{r}), \quad (19)$$

where for  $\rho_c$  we restrict the sum  $\sum_n$  in Eq. (18) to contain only those bands that are assumed to be fully filled ( $f_n(\mathbf{k}) = 1$ ) during the entire SCF procedure.  $\rho_c$  contains contributions to the electron density from the majority of bands – these terms are evaluated on-the-fly after the diagonalization independently for each  $\mathbf{k}$  point without the need to store the full coefficient matrices. The remaining terms in the density are incorporated in  $\rho_v$  and calculated in a separate loop over  $\mathbf{k}$  after all  $\varepsilon_n(\mathbf{k})$  and  $f_n(\mathbf{k})$  are known, which allows for a small number of partially filled bands ( $f_n(\mathbf{k})$  can vary across  $\mathbf{k}$ ). The coefficients  $c_n^\mu(\mathbf{k})$  needed for  $\rho_v$  can be stored in memory as they form narrow rectangular matrices with only one dimension increasing with the system size. In addition, each MPI process only needs to keep the coefficients for the subset of  $\mathbf{k}$  points that the process handles, which is advantageous for multinode calculations within the distributed-memory architecture since the coefficients do not need to be shared or communicated among nodes. The parallel scheme described here enables seamless all-electron fully relativistic 4c calculations of band structures or density of states with a large number of  $\mathbf{k}$  points using thousands of cores.

### C. Evaluation of $\mathbb{Z}_2$ invariant

The QSH phase of 2D materials with time-reversal symmetry is characterized by a nontrivial topological order associated with a nonzero  $\mathbb{Z}_2$  index [131]. Identification of topological materials from numerical simulations is not straightforward [132]. However, for systems with inversion symmetry, the calculation of the  $\mathbb{Z}_2$  invariant can be simplified using Fu and Kane’s method [118] based on the knowledge of the parity of the Bloch wave functions of the bulk crystal at the time-reversal invariant momenta (TRIM) of the Brillouin zone. In this section, we describe how the  $\mathbb{Z}_2$  invariant is calculated in the 4c real-space GTO basis.

First, we discuss the construction of the momentum-space parity operator  $P_{\mu\mu'}(\mathbf{k})$ . Let  $\mathcal{I}$  denote the space-inversion operator with the inversion center at  $\mathbf{G}$ , defined by its action on a scalar function  $f$  as  $\mathcal{I}f(\mathbf{r}) \equiv f(2\mathbf{G} - \mathbf{r})$ . From the requirement that the parity-transformed bispinor wave function  $\psi(\mathbf{r}, t)$  satisfies the same Dirac equation, it is possible to identify the form of the 4c parity operator  $\hat{P}$  as

$$\hat{P}\psi(\mathbf{r}, t) = \eta\beta\psi(2\mathbf{G} - \mathbf{r}, t) \equiv \eta\beta\mathcal{I}\psi(\mathbf{r}, t), \quad (20)$$

where  $\beta = \text{diag}(\mathbb{I}_2, -\mathbb{I}_2)$  and  $\eta$  is an arbitrary phase factor ( $|\eta| = 1$ ) that can be introduced by the parity transformation. Neglecting the phase gives  $\hat{P} = \beta\mathcal{I}$ . The 4c matrix form of the parity operator is obtained by realizing that  $\mathcal{I}\mathbf{p}\mathcal{I}^\dagger = -\mathbf{p}$  and letting  $\hat{P}$  act on the RKB basis

in Eq. (6), *i.e.*

$$\hat{P}\chi_\mu \equiv \hat{P} \begin{pmatrix} \mathbb{I}_2 & 0_2 \\ 0_2 & \frac{1}{2c}\boldsymbol{\sigma} \cdot \mathbf{p} \end{pmatrix} g_\mu = \begin{pmatrix} \mathbb{I}_2 & 0_2 \\ 0_2 & \frac{1}{2c}\boldsymbol{\sigma} \cdot \mathbf{p} \end{pmatrix} \mathcal{I}g_\mu. \quad (21)$$

It follows that the parity matrix  $P_{\mu\mu'}(\mathbf{k})$  can be obtained using Eq. (4b) for the overlap matrix with an additional application of the inversion  $\mathcal{I}$  on the scalar basis function  $g_{\mu'}$ . For an orbital from Eq. (7) with angular momentum number  $l$  that is centered at  $\mathbf{A}$  (which here denotes the position of an atom  $\mathbf{A}_\mu$  in a unit cell  $\mathbf{R}$ ), this inversion gives

$$\mathcal{I}g_\mu(\mathbf{r} - \mathbf{A}) = (-1)^l g_\mu(\mathbf{r} + \mathbf{A} - 2\mathbf{G}). \quad (22)$$

Finally, the  $\mathbb{Z}_2$  invariant is calculated using the eigenvalues  $\xi_{2m}$  of the parity  $P_{\mu\mu'}(\mathbf{k})$  as [118]

$$(-1)^\nu = \prod_{i=1}^4 \prod_{m=1}^N \xi_{2m}(\Gamma_i), \quad (23)$$

where  $N$  is the number of occupied Kramers pairs, and  $\Gamma_i$  labels the four TRIMs in 2D.

We conclude this section by noting a few considerations required for a numerically stable and reliable calculation of the parity matrix and its eigenvalues when using the method outlined here. First, the sparse matrix storage scheme outlined in Section IV A based on the locality of basis function products  $\chi_\mu^\dagger(\mathbf{r})\chi_{\mu'}(\mathbf{r} - \mathbf{R})$  needs to be modified to respect the nonlocal nature of the inversion operator. Specifically, the list of significant elements of the inversion matrix is not the same as for the overlap matrix, but is related to it via reflection. Likewise, it must be ensured that the atomic basis set chosen for the inversion-equivalent atoms is the same. Finally, it is not automatically guaranteed that the Bloch functions in Eq. (2) that are solutions of the DKS equation are also eigenfunctions of the parity operator for Bloch states with degenerate energies. Parity eigenvalues can be obtained by diagonalizing the sub-blocks of the parity matrix that correspond to these degenerate energy levels. However, in numerical simulations, energy values obtained from diagonalization routines are not necessarily exactly degenerate, but rather appear as near-degenerate. At the same time, eigenvectors corresponding to these near-degenerate levels are not uniquely defined. Hence, we introduced an energy threshold that identifies the degeneracies.

### DATA AVAILABILITY

The data presented in this study as well as the scripts used for pre- and post-processing of the input and output files are available in the [ZENODO public repository](#) [133].

## CODE AVAILABILITY

The RESPECT code used in this study is available at [www.respectprogram.org](http://www.respectprogram.org) upon a reasonable request free of charge.

## ACKNOWLEDGMENTS

This work was supported by the Research Council of Norway through its Centres of Excellence scheme (Grant No. 262695), a Research Grant (Grant No. 315822), and its Mobility Grant scheme (Grant No. 301864), as well as the use of computational resources provided

by UNINETT Sigma2 – The National Infrastructure for High Performance Computing and Data Storage in Norway (Grant No. NN4654K). In addition, this project received funding from the European Union’s Horizon 2020 research and innovation program under the Marie Skłodowska-Curie Grant Agreement No. 945478 (SASPRO2), and the Slovak Research and Development Agency (Grant No. APVV-21-0497). The work at Northeastern University was supported by the Air Force Office of Scientific Research under award number FA9550-20-1-0322 and benefited from the computational resources of Northeastern University’s Advanced Scientific Computation Center (ASCC) and the Discovery Cluster.

- 
- [1] S. Z. Butler, S. M. Hollen, L. Cao, Y. Cui, J. A. Gupta, H. R. Gutiérrez, T. F. Heinz, S. S. Hong, J. Huang, A. F. Ismach, *et al.*, Progress, challenges, and opportunities in two-dimensional materials beyond graphene, *ACS nano* **7**, 2898 (2013).
- [2] W. Han, Perspectives for spintronics in 2D materials, *APL Mater.* **4**, 032401 (2016).
- [3] R. Frindt, Single crystals of MoS<sub>2</sub> several molecular layers thick, *J. Appl. Phys.* **37**, 1928 (1966).
- [4] A. K. Geim and K. S. Novoselov, The rise of graphene, *Nat. Mater.* **6**, 183 (2007).
- [5] S. D. Sarma, S. Adam, E. Hwang, and E. Rossi, Electronic transport in two-dimensional graphene, *Rev. Mod. Phys.* **83**, 407 (2011).
- [6] P. Miró, M. Audiffred, and T. Heine, An atlas of two-dimensional materials, *Chem. Soc. Rev.* **43**, 6537 (2014).
- [7] N. Tombros, C. Jozsa, M. Popinciuc, H. T. Jonkman, and B. J. Van Wees, Electronic spin transport and spin precession in single graphene layers at room temperature, *Nature* **448**, 571 (2007).
- [8] X. Li, J. T. Mullen, Z. Jin, K. M. Borysenko, M. B. Nardelli, and K. W. Kim, Intrinsic electrical transport properties of monolayer silicene and MoS<sub>2</sub> from first principles, *Phys. Rev. B* **87**, 115418 (2013).
- [9] C. L. Kane and E. J. Mele, Quantum spin Hall effect in graphene, *Phys. Rev. Lett.* **95**, 226801 (2005).
- [10] C.-C. Liu, W. Feng, and Y. Yao, Quantum spin Hall effect in silicene and two-dimensional germanium, *Phys. Rev. Lett.* **107**, 076802 (2011).
- [11] X. Qian, J. Liu, L. Fu, and J. Li, Quantum spin Hall effect in two-dimensional transition metal dichalcogenides, *Science* **346**, 1344 (2014).
- [12] Y. Hor, A. Richardella, P. Roushan, Y. Xia, J. Checkelsky, A. Yazdani, M. Hasan, N. P. Ong, and R. J. Cava, *p*-type Bi<sub>2</sub>Se<sub>3</sub> for topological insulator and low-temperature thermoelectric applications, *Phys. Rev. B* **79**, 195208 (2009).
- [13] Q. H. Wang, K. Kalantar-Zadeh, A. Kis, J. N. Coleman, and M. S. Strano, Electronics and optoelectronics of two-dimensional transition metal dichalcogenides, *Nat. Nanotechnol.* **7**, 699 (2012).
- [14] J. Nilsson, A. Akhmerov, and C. Beenakker, Splitting of a Cooper pair by a pair of Majorana bound states, *Phys. Rev. Lett.* **101**, 120403 (2008).
- [15] L. Fu and C. L. Kane, Josephson current and noise at a superconductor/quantum-spin-Hall-insulator/superconductor junction, *Phys. Rev. B* **79**, 161408 (2009).
- [16] B. Radisavljevic, A. Radenovic, J. Brivio, V. Giacometti, and A. Kis, Single-layer MoS<sub>2</sub> transistors, *Nat. Nanotechnol.* **6**, 147 (2011).
- [17] L. Britnell, R. Gorbachev, R. Jalil, B. Belle, F. Schedin, A. Mishchenko, T. Georgiou, M. Katsnelson, L. Eaves, S. Morozov, *et al.*, Field-effect tunneling transistor based on vertical graphene heterostructures, *Science* **335**, 947 (2012).
- [18] P. Solomon, B. Bryce, M. Kuroda, R. Keech, S. Shetty, T. Shaw, M. Copel, L.-W. Hung, A. Schrott, C. Armstrong, *et al.*, Pathway to the piezoelectronic transduction logic device, *Nano Lett.* **15**, 2391 (2015).
- [19] H. Li, A. W. Contryman, X. Qian, S. M. Ardakani, Y. Gong, X. Wang, J. M. Weisse, C. H. Lee, J. Zhao, P. M. Ajayan, *et al.*, Optoelectronic crystal of artificial atoms in strain-textured molybdenum disulphide, *Nat. Commun.* **6**, 1 (2015).
- [20] V. W. Brar, R. Decker, H.-M. Solowan, Y. Wang, L. Maserati, K. T. Chan, H. Lee, Ç. O. Girit, A. Zettl, S. G. Louie, *et al.*, Gate-controlled ionization and screening of cobalt adatoms on a graphene surface, *Nat. Phys.* **7**, 43 (2011).
- [21] F. D. Natterer, F. Patthey, and H. Brune, Ring state for single transition metal atoms on boron nitride on Rh (111), *Phys. Rev. Lett.* **109**, 066101 (2012).
- [22] W.-F. Tsai, C.-Y. Huang, T.-R. Chang, H. Lin, H.-T. Jeng, and A. Bansil, Gated silicene as a tunable source of nearly 100% spin-polarized electrons, *Nat. Commun.* **4**, 1 (2013).
- [23] L. Ponomarenko, A. Geim, A. Zhukov, R. Jalil, S. Morozov, K. Novoselov, I. Grigorieva, E. Hill, V. Cheianov, V. Fal’ko, *et al.*, Tunable metal–insulator transition in double-layer graphene heterostructures, *Nat. Phys.* **7**, 958 (2011).
- [24] A. K. Geim and I. V. Grigorieva, Van der Waals heterostructures, *Nature* **499**, 419 (2013).
- [25] S. Haigh, A. Gholinia, R. Jalil, S. Romani, L. Britnell, D. Elias, K. Novoselov, L. Ponomarenko, A. Geim, and R. Gorbachev, Cross-sectional imaging of individual lay-

- ers and buried interfaces of graphene-based heterostructures and superlattices, *Nat. Mater.* **11**, 764 (2012).
- [26] S. Manzeli, D. Ovchinnikov, D. Pasquier, O. V. Yazyev, and A. Kis, 2D transition metal dichalcogenides, *Nat. Rev. Mater.* **2**, 1 (2017).
- [27] K. Kang, T. Li, E. Sohn, J. Shan, and K. F. Mak, Non-linear anomalous Hall effect in few-layer WTe<sub>2</sub>, *Nat. Mater.* **18**, 324 (2019).
- [28] Z. Wang, B. J. Wieder, J. Li, B. Yan, and B. A. Bernevig, Higher-Order Topology, Monopole Nodal Lines, and the Origin of Large Fermi Arcs in Transition Metal Dichalcogenides XTe<sub>2</sub> (X = Mo, W), *Phys. Rev. Lett.* **123**, 186401 (2019).
- [29] Z. Zhu, Y. Cheng, and U. Schwingenschlögl, Giant spin-orbit-induced spin splitting in two-dimensional transition-metal dichalcogenide semiconductors, *Phys. Rev. B* **84**, 153402 (2011).
- [30] J. Wilson, F. Di Salvo, and S. Mahajan, Charge-density waves in metallic, layered, transition-metal dichalcogenides, *Phys. Rev. Lett.* **32**, 882 (1974).
- [31] F. Flicker and J. Van Wezel, Charge order from orbital-dependent coupling evidenced by NbSe<sub>2</sub>, *Nat. Commun.* **6**, 1 (2015).
- [32] X. Zhu, Y. Guo, H. Cheng, J. Dai, X. An, J. Zhao, K. Tian, S. Wei, X. C. Zeng, C. Wu, *et al.*, Signature of coexistence of superconductivity and ferromagnetism in two-dimensional NbSe<sub>2</sub> triggered by surface molecular adsorption, *Nat. Commun.* **7**, 1 (2016).
- [33] D. Xiao, G.-B. Liu, W. Feng, X. Xu, and W. Yao, Coupled spin and valley physics in monolayers of MoS<sub>2</sub> and other group-VI dichalcogenides, *Phys. Rev. Lett.* **108**, 196802 (2012).
- [34] K. F. Mak, K. L. McGill, J. Park, and P. L. McEuen, The valley Hall effect in MoS<sub>2</sub> transistors, *Science* **344**, 1489 (2014).
- [35] A. Pulkin and O. V. Yazyev, Spin-and valley-polarized transport across line defects in monolayer MoS<sub>2</sub>, *Phys. Rev. B* **93**, 041419 (2016).
- [36] X. Xu, W. Yao, D. Xiao, and T. F. Heinz, Spin and pseudospins in layered transition metal dichalcogenides, *Nat. Phys.* **10**, 343 (2014).
- [37] B. T. Zhou, N. F. Yuan, H.-L. Jiang, and K. T. Law, Ising superconductivity and Majorana fermions in transition-metal dichalcogenides, *Phys. Rev. B* **93**, 180501 (2016).
- [38] W.-Y. He, B. T. Zhou, J. J. He, N. F. Yuan, T. Zhang, and K. T. Law, Magnetic field driven nodal topological superconductivity in monolayer transition metal dichalcogenides, *Commun. Phys.* **1**, 1 (2018).
- [39] J.-Y. Tsai, J. Pan, H. Lin, A. Bansil, and Q. Yan, Antisite defect qubits in monolayer transition metal dichalcogenides, *Nat. Commun.* **13**, 1 (2022).
- [40] P. A. Dirac, The quantum theory of the electron, *Proc. R. Soc. A* **117**, 610 (1928).
- [41] T. Saue and T. Helgaker, Four-component relativistic Kohn-Sham theory, *J. Comput. Chem.* **23**, 814 (2002).
- [42] L. Belpassi, L. Storchi, H. M. Quiney, and F. Tarantelli, Recent advances and perspectives in four-component Dirac-Kohn-Sham calculations, *Phys. Chem. Chem. Phys.* **13**, 12368 (2011).
- [43] T. Saue, Relativistic Hamiltonians for chemistry: a primer, *ChemPhysChem* **12**, 3077 (2011).
- [44] W. Liu, Advances in relativistic molecular quantum mechanics, *Phys. Rep.* **537**, 59 (2014).
- [45] P. Hohenberg and W. Kohn, Inhomogeneous electron gas, *Phys. Rev.* **136**, B864 (1964).
- [46] W. Kohn and L. J. Sham, Self-consistent equations including exchange and correlation effects, *Phys. Rev.* **140**, A1133 (1965).
- [47] C.-N. Yeh, A. Shee, Q. Sun, E. Gull, and D. Zgid, Relativistic self-consistent GW: Exact two-component formalism with one-electron approximation for solids, *Phys. Rev. B* **106**, 085121 (2022).
- [48] A. Rajagopal and J. Callaway, Inhomogeneous electron gas, *Phys. Rev. B* **7**, 1912 (1973).
- [49] S. Komorovsky, M. Repisky, O. L. Malkina, V. G. Malkin, I. Malkin Ondik, and M. Kaupp, A fully relativistic method for calculation of nuclear magnetic shielding tensors with a restricted magnetically balanced basis in the framework of the matrix Dirac-Kohn-Sham equation, *J. Chem. Phys.* **128**, 104101 (2008).
- [50] E. Engel, Relativistic Density Functional Theory: Foundations and Basic Formalism, in *Theoretical and computational chemistry*, Vol. 11, edited by P. Schwerdtfeger (Elsevier, 2002) Chap. 10, pp. 523–621.
- [51] K. G. Dyall and K. Faegri, *Introduction to relativistic quantum chemistry* (Oxford University Press, New York, 2007) pp. 268–274.
- [52] T. Saue, K. Fægri, T. Helgaker, and O. Gropen, Principles of direct 4-component relativistic SCF: application to caesium auride, *Mol. Phys.* **91**, 937 (1997).
- [53] L. Konecny, M. Kadek, S. Komorovsky, K. Ruud, and M. Repisky, Resolution-of-identity accelerated relativistic two- and four-component electron dynamics approach to chiroptical spectroscopies, *J. Chem. Phys.* **149**, 204104 (2018).
- [54] M. Kadek, M. Repisky, and K. Ruud, All-electron fully relativistic Kohn-Sham theory for solids based on the Dirac-Coulomb Hamiltonian and Gaussian-type functions, *Phys. Rev. B* **99**, 205103 (2019).
- [55] M. Repisky, S. Komorovsky, M. Kadek, L. Konecny, U. Ekström, E. Malkin, M. Kaupp, K. Ruud, O. L. Malkina, and V. G. Malkin, ReSpect: Relativistic spectroscopy DFT program package, *J. Chem. Phys.* **152**, 184101 (2020).
- [56] L. Kleinman, Relativistic norm-conserving pseudopotential, *Phys. Rev. B* **21**, 2630 (1980).
- [57] G. B. Bachelet and M. Schlüter, Relativistic norm-conserving pseudopotentials, *Phys. Rev. B* **25**, 2103 (1982).
- [58] A. Dal Corso and A. M. Conte, Spin-orbit coupling with ultrasoft pseudopotentials: Application to Au and Pt, *Phys. Rev. B* **71**, 115106 (2005).
- [59] P. Nichols, N. Govind, E. J. Bylaska, and W. A. De Jong, Gaussian Basis Set and Planewave Relativistic Spin-Orbit Methods in NWChem, *J. Chem. Theory Comput.* **5**, 491 (2009).
- [60] A. Dal Corso, Projector augmented-wave method: Application to relativistic spin-density functional theory, *Phys. Rev. B* **82**, 075116 (2010).
- [61] G. Bihlmayer, Y. M. Koroteev, P. M. Echenique, E. V. Chulkov, and S. Blügel, The Rashba-effect at metallic surfaces, *Surf. Sci.* **600**, 3888 (2006).
- [62] K. Ghosh, H. Ma, M. Onizhuk, V. Gavini, and G. Galli, Spin-spin interactions in defects in solids from mixed all-electron and pseudopotential first-principles calculations, *Npj Comput. Mater.* **7**, 1 (2021).

- [63] M. Gmitra, S. Konschuh, C. Ertler, C. Ambrosch-Draxl, and J. Fabian, Band-structure topologies of graphene: Spin-orbit coupling effects from first principles, *Phys. Rev. B* **80**, 235431 (2009).
- [64] J. Sichau, M. Prada, T. Anlauf, T. Lyon, B. Bosnjak, L. Tiemann, and R. Blick, Resonance microwave measurements of an intrinsic spin-orbit coupling gap in graphene: A possible indication of a topological state, *Phys. Rev. Lett.* **122**, 046403 (2019).
- [65] O. K. Andersen, Linear methods in band theory, *Phys. Rev. B* **12**, 3060 (1975).
- [66] A. MacDonald, W. Pickett, and D. Koelling, A linearised relativistic augmented-plane-wave method utilising approximate pure spin basis functions, *J. Phys. C* **13**, 2675 (1980).
- [67] E. Wimmer, H. Krakauer, M. Weinert, and A. Freeman, Full-potential self-consistent linearized-augmented-plane-wave method for calculating the electronic structure of molecules and surfaces: O<sub>2</sub> molecule, *Phys. Rev. B* **24**, 864 (1981).
- [68] N. Christensen, Spin-orbit projected d densities-of-states of Pd, Ag, Pt, and Au, *J. Phys. F* **8**, L51 (1978).
- [69] H. Ebert, P. Strange, and B. L. Gyorffy, Spin-polarized relativistic LMTO method, *J. Appl. Phys.* **63**, 3052 (1988).
- [70] D. A. Rehn, J. M. Wills, T. E. Battelle, and A. E. Mattsson, Dirac's equation and its implications for density functional theory based calculations of materials containing heavy elements, *Phys. Rev. B* **101**, 085114 (2020).
- [71] W. P. Huhn and V. Blum, One-hundred-three compound band-structure benchmark of post-self-consistent spin-orbit coupling treatments in density functional theory, *Phys. Rev. Mater.* **1**, 033803 (2017).
- [72] S. Suzuki and K. Nakao, A fully relativistic full-potential LCAO method for solids, *J. Phys. Soc. Jpn.* **68**, 1982 (1999).
- [73] K. Koepf and H. Eschrig, Full-potential nonorthogonal local-orbital minimum-basis band-structure scheme, *Phys. Rev. B* **59**, 1743 (1999).
- [74] R. Zhao, V. W.-z. Yu, K. Zhang, Y. Xiao, Y. Zhang, and V. Blum, Quasi-four-component method with numeric atom-centered orbitals for relativistic density functional simulations of molecules and solids, *Phys. Rev. B* **103**, 245144 (2021).
- [75] P. Philipson, E. Van Lenthe, J. Snijders, and E. Baerends, Relativistic calculations on the adsorption of CO on the (111) surfaces of Ni, Pd, and Pt within the zeroth-order regular approximation, *Phys. Rev. B* **56**, 13556 (1997).
- [76] R. Zhao, Y. Zhang, Y. Xiao, and W. Liu, Exact two-component relativistic energy band theory and application, *J. Chem. Phys.* **144**, 044105 (2016).
- [77] J. Boettger and S. Trickey, First-principles calculation of the spin-orbit splitting in graphene, *Phys. Rev. B* **75**, 121402 (2007).
- [78] C. Pisani, M. Schütz, S. Casassa, D. Usvyat, L. Maschio, M. Lorenz, and A. Erba, Cryscor: a program for the post-Hartree-Fock treatment of periodic systems, *Phys. Chem. Chem. Phys.* **14**, 7615 (2012).
- [79] G. H. Booth, T. Tsatsoulis, G. K.-L. Chan, and A. Grüneis, From plane waves to local Gaussians for the simulation of correlated periodic systems, *J. Chem. Phys.* **145**, 084111 (2016).
- [80] J. McClain, Q. Sun, G. K.-L. Chan, and T. C. Berkelbach, Gaussian-based coupled-cluster theory for the ground-state and band structure of solids, *J. Chem. Theory Comput.* **13**, 1209 (2017).
- [81] E. Rebolini, G. Baardsen, A. S. Hansen, K. R. Leikanger, and T. B. Pedersen, Divide-Expand-Consolidate Second-Order Møller-Plesset Theory with Periodic Boundary Conditions, *J. Chem. Theory Comput.* **14**, 2427 (2018).
- [82] J. M. Crowley, J. Tahir-Kheli, and W. A. Goddard III, Resolution of the band gap prediction problem for materials design, *J. Phys. Chem. Lett.* **7**, 1198 (2016).
- [83] K. N. Kudin and G. E. Scuseria, Linear-scaling density-functional theory with Gaussian orbitals and periodic boundary conditions: Efficient evaluation of energy and forces via the fast multipole method, *Phys. Rev. B* **61**, 16444 (2000).
- [84] R. Lazarski, A. M. Burow, and M. Sierka, Density functional theory for molecular and periodic systems using density fitting and continuous fast multipole methods, *J. Chem. Theory Comput.* **11**, 3029 (2015).
- [85] M. Kadec, L. Konecny, B. Gao, M. Repisky, and K. Ruud, X-ray absorption resonances near L<sub>2</sub>, 3-edges from real-time propagation of the Dirac-Kohn-Sham density matrix, *Phys. Chem. Chem. Phys.* **17**, 22566 (2015).
- [86] S. Komorovský, M. Repiský, O. L. Malkina, V. G. Malkin, I. Malkin, and M. Kaupp, Resolution of identity Dirac-Kohn-Sham method using the large component only: Calculations of g-tensor and hyperfine tensor, *J. Chem. Phys.* **124**, 084108 (2006).
- [87] M. Repiský, S. Komorovský, O. L. Malkina, and V. G. Malkin, Restricted magnetically balanced basis applied for relativistic calculations of indirect nuclear spin-spin coupling tensors in the matrix Dirac-Kohn-Sham framework, *Chem. Phys.* **356**, 236 (2009).
- [88] C. Pisani and R. Dovesi, Exact-exchange Hartree-Fock calculations for periodic systems. I. Illustration of the method, *Int. J. Quantum Chem.* **17**, 501 (1980).
- [89] R. Dovesi, C. Pisani, C. Roetti, and V. Saunders, Treatment of Coulomb interactions in Hartree-Fock calculations of periodic systems, *Phys. Rev. B* **28**, 5781 (1983).
- [90] R. Dovesi, F. Pascale, B. Civalleri, K. Doll, N. M. Harrison, I. Bush, P. D'arco, Y. Noël, M. Rérat, P. Carbonniere, *et al.*, The CRYSTAL code, 1976-2020 and beyond, a long story, *J. Chem. Phys.* **152**, 204111 (2020).
- [91] Q. Sun, X. Zhang, S. Banerjee, P. Bao, M. Barbry, N. S. Blunt, N. A. Bogdanov, G. H. Booth, J. Chen, Z.-H. Cui, *et al.*, Recent developments in the PySCF program package, *J. Chem. Phys.* **153**, 024109 (2020).
- [92] S. Suhai, P. Bagus, and J. Ladik, An error analysis for Hartree-Fock crystal orbital calculations, *Chem. Phys.* **68**, 467 (1982).
- [93] M. F. Peintinger, D. V. Oliveira, and T. Bredow, Consistent Gaussian basis sets of triple-zeta valence with polarization quality for solid-state calculations, *J. Comput. Chem.* **34**, 451 (2013).
- [94] T. Zhu and G. K.-L. Chan, All-electron Gaussian-based G<sub>0</sub>W<sub>0</sub> for valence and core excitation energies of periodic systems, *J. Chem. Theory Comput.* **17**, 727 (2021).
- [95] J. E. Peralta, J. Uddin, and G. E. Scuseria, Scalar relativistic all-electron density functional calculations on periodic systems, *J. Chem. Phys.* **122**, 084108 (2005).

- [96] D. Usvyat, B. Civalleri, L. Maschio, R. Dovesi, C. Pisani, and M. Schütz, Approaching the theoretical limit in periodic local MP2 calculations with atomic-orbital basis sets: the case of LiH, *J. Chem. Phys.* **134**, 214105 (2011).
- [97] J. K. Perry, J. Tahir-Kheli, and W. A. Goddard III, Antiferromagnetic band structure of La<sub>2</sub>CuO<sub>4</sub>: Becke-3-Lee-Yang-Parr calculations, *Phys. Rev. B* **63**, 144510 (2001).
- [98] L. E. Daga, B. Civalleri, and L. Maschio, Gaussian basis sets for crystalline solids: All-purpose basis set libraries vs system-specific optimizations, *J. Chem. Theory Comput.* **16**, 2192 (2020).
- [99] F. Jensen, Analysis of energy-optimized gaussian basis sets for condensed phase density functional calculations, *Theor. Chem. Acc.* **132**, 1 (2013).
- [100] R. E. Stanton and S. Havriliak, Kinetic balance: A partial solution to the problem of variational safety in Dirac calculations, *J. Chem. Phys.* **81**, 1910 (1984).
- [101] E. J. Baerends, D. Ellis, and P. Ros, Self-consistent molecular Hartree-Fock-Slater calculations I. The computational procedure, *Chem. Phys.* **2**, 41 (1973).
- [102] Y. Jung, A. Sodt, P. M. Gill, and M. Head-Gordon, Auxiliary basis expansions for large-scale electronic structure calculations, *Proc. Natl. Acad. Sci. U.S.A.* **102**, 6692 (2005).
- [103] Š. Varga, Long-range analysis of density fitting in extended systems, *Int. J. Quantum Chem.* **108**, 1518 (2008).
- [104] G. Te Velde and E. Baerends, Precise density-functional method for periodic structures, *Phys. Rev. B* **44**, 7888 (1991).
- [105] G. Kresse and J. Furthmüller, Efficient iterative schemes for ab initio total-energy calculations using a plane-wave basis set, *Phys. Rev. B* **54**, 11169 (1996).
- [106] J. P. Perdew, K. Burke, and M. Ernzerhof, Generalized gradient approximation made simple, *Phys. Rev. Lett.* **77**, 3865 (1996).
- [107] L. Visscher and K. G. Dyall, Dirac-Fock atomic electronic structure calculations using different nuclear charge distributions, *At. Data Nucl. Data Tables* **67**, 207 (1997).
- [108] K. G. Dyall, Relativistic double-zeta, triple-zeta, and quadruple-zeta basis sets for the 4d elements Y-Cd, *Theor. Chem. Acc.* **117**, 483 (2007).
- [109] K. G. Dyall, Relativistic double-zeta, triple-zeta, and quadruple-zeta basis sets for the 5d elements Hf-Hg, *Theor. Chem. Acc.* **112**, 403 (2004).
- [110] K. G. Dyall and A. S. Gomes, Revised relativistic basis sets for the 5d elements Hf-Hg, *Theor. Chem. Acc.* **125**, 97 (2010).
- [111] K. G. Dyall, Relativistic and nonrelativistic finite nucleus optimized triple-zeta basis sets for the 4p, 5p and 6p elements, *Theor. Chem. Acc.* **108**, 335 (2002).
- [112] K. G. Dyall, Relativistic quadruple-zeta and revised triple-zeta and double-zeta basis sets for the 4p, 5p, and 6p elements, *Theor. Chem. Acc.* **115**, 441 (2006).
- [113] K. Kořmider, J. W. González, and J. Fernández-Rossier, Large spin splitting in the conduction band of transition metal dichalcogenide monolayers, *Phys. Rev. B* **88**, 245436 (2013).
- [114] E. Van Lenthe, R. Van Leeuwen, E. Baerends, and J. Snijders, Relativistic regular two-component Hamiltonians, *Int. J. Quantum Chem.* **57**, 281 (1996).
- [115] S. Grimme, J. Antony, S. Ehrlich, and H. Krieg, A consistent and accurate ab initio parametrization of density functional dispersion correction (DFT-D) for the 94 elements H-Pu, *J. Chem. Phys.* **132**, 154104 (2010).
- [116] W. Setyawan and S. Curtarolo, High-throughput electronic band structure calculations: Challenges and tools, *Comput. Mater. Sci.* **49**, 299 (2010).
- [117] G. Eda, T. Fujita, H. Yamaguchi, D. Voiry, M. Chen, and M. Chhowalla, Coherent atomic and electronic heterostructures of single-layer MoS<sub>2</sub>, *ACS nano* **6**, 7311 (2012).
- [118] L. Fu and C. L. Kane, Topological insulators with inversion symmetry, *Phys. Rev. B* **76**, 045302 (2007).
- [119] W. Schwarz and H. Wallmeier, Basis set expansions of relativistic molecular wave equations, *Mol. Phys.* **46**, 1045 (1982).
- [120] K. G. Dyall, An exact separation of the spin-free and spin-dependent terms of the Dirac-Coulomb-Breit Hamiltonian, *J. Chem. Phys.* **100**, 2118 (1994).
- [121] M. Repisky, L. Konecny, M. Kadek, S. Komorovsky, O. L. Malkin, V. G. Malkin, and K. Ruud, Excitation energies from real-time propagation of the four-component Dirac-Kohn-Sham equation, *J. Chem. Theory Comput.* **11**, 980 (2015).
- [122] S. G. Balasubramani, G. P. Chen, S. Coriani, M. Diedenhofen, M. S. Frank, Y. J. Franzke, F. Furche, R. Grotjahn, M. E. Harding, C. Hättig, *et al.*, TURBO-MOLE: Modular program suite for ab initio quantum-chemical and condensed-matter simulations, *J. Chem. Phys.* **152**, 184107 (2020).
- [123] E. Apra, E. J. Bylaska, W. A. De Jong, N. Govind, K. Kowalski, T. P. Straatsma, M. Valiev, H. J. van Dam, Y. Alexeev, J. Anchell, *et al.*, NWChem: Past, present, and future, *J. Chem. Phys.* **152**, 184102 (2020).
- [124] T. Saue, R. Bast, A. S. P. Gomes, H. J. A. Jensen, L. Visscher, I. A. Aucar, R. Di Remigio, K. G. Dyall, E. Eliav, E. Fasshauer, *et al.*, The DIRAC code for relativistic molecular calculations, *J. Chem. Phys.* **152**, 204104 (2020).
- [125] J. M. H. Olsen, S. Reine, O. Vahtras, E. Kjøllgren, P. Reinholdt, K. O. Hjørth Dundas, X. Li, J. Cukras, M. Ringholm, E. D. Hedegård, *et al.*, Dalton Project: A Python platform for molecular-and electronic-structure simulations of complex systems, *J. Chem. Phys.* **152**, 214115 (2020).
- [126] L. Belpassi, M. De Santis, H. M. Quiney, F. Tarantelli, and L. Storchi, BERTHA: Implementation of a four-component Dirac-Kohn-Sham relativistic framework, *J. Chem. Phys.* **152**, 164118 (2020).
- [127] S. Obara and A. Saika, Efficient recursive computation of molecular integrals over Cartesian Gaussian functions, *J. Chem. Phys.* **84**, 3963 (1986).
- [128] S. F. Boys, Electronic wave functions-I. A general method of calculation for the stationary states of any molecular system, *Proc. R. Soc. A* **200**, 542 (1950).
- [129] M. Sierka, A. Hogekamp, and R. Ahlrichs, Fast evaluation of the Coulomb potential for electron densities using multipole accelerated resolution of identity approximation, *J. Chem. Phys.* **118**, 9136 (2003).
- [130] Q. Sun, T. C. Berkelbach, J. D. McClain, and G. K.-L. Chan, Gaussian and plane-wave mixed density fitting for periodic systems, *J. Chem. Phys.* **147**, 164119 (2017).

- [131] C. L. Kane and E. J. Mele,  $Z_2$  topological order and the quantum spin hall effect, *Phys. Rev. Lett.* **95**, 146802 (2005).
- [132] D. Gresch, G. Autes, O. V. Yazyev, M. Troyer, D. Vanderbilt, B. A. Bernevig, and A. A. Soluyanov, Z2Pack: Numerical implementation of hybrid Wannier centers for identifying topological materials, *Phys. Rev. B* **95**, 075146 (2017).
- [133] M. Kadek, B. Wang, M. Joosten, W.-C. Chiu, F. Mairesse, M. Repisky, K. Ruud, and A. Bansil, Dataset for "Band structures and  $Z_2$  invariant of 2D transition metal dichalcogenides from fully relativistic Dirac-Kohn-Sham theory using Gaussian-type orbitals", ZENODO (2022).

# Supplementary Materials for

## Band structures and $\mathbb{Z}_2$ invariants of 2D transition metal dichalcogenide monolayers from fully-relativistic Dirac–Kohn–Sham theory using Gaussian-type orbitals

Marius Kadek,<sup>1,2,\*</sup> Baokai Wang,<sup>1</sup> Marc Joosten,<sup>2</sup> Wei-Chi Chiu,<sup>1</sup>  
Francois Mairesse,<sup>3</sup> Michal Repisky,<sup>2</sup> Kenneth Ruud,<sup>2</sup> and Arun Bansil<sup>1</sup>

<sup>1</sup>*Department of Physics, Northeastern University,  
Boston, Massachusetts 02115, USA*

<sup>2</sup>*Hylleraas Centre for Quantum Molecular Sciences,  
UiT The Arctic University of Norway, N-9037 Tromsø, Norway*

<sup>3</sup>*Laboratory of Theoretical Chemistry,  
University of Namur, B-5000 Namur, Belgium*

(Dated: February 2, 2023)

TABLE SI.: Direct SOC-induced band gaps between the valence and conduction bands of  $\text{MX}_2$  in the 1T phase evaluated at the  $K$  point.

	$K$ - $K$ gap (eV)
MoS <sub>2</sub>	0.079
MoSe <sub>2</sub>	0.114
MoTe <sub>2</sub>	0.138
WS <sub>2</sub>	0.175
WSe <sub>2</sub>	0.205
WTe <sub>2</sub>	0.173

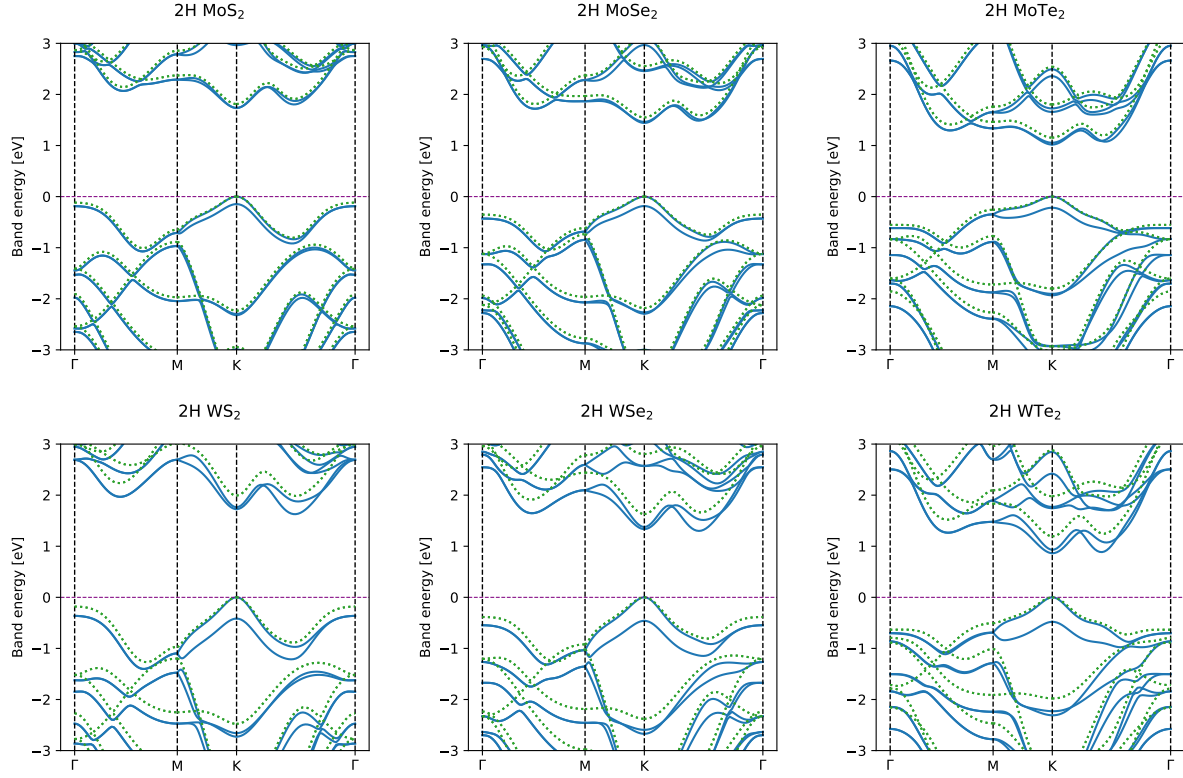


FIG. S1:. Band structures of  $\text{MX}_2$  monolayers in the 2H phase obtained from the RESPECT code at the scalar-relativistic (dashed lines, no SOC) and fully-relativistic (full lines, with SOC) levels of the theory. The horizontal dashed black line separates the occupied and the vacant states, and was placed in the top of the valence band for insulating systems. The unit cell-structure and lattice parameters were taken from Ref. ? .

---

\* [marius.kadek@uit.no](mailto:marius.kadek@uit.no)

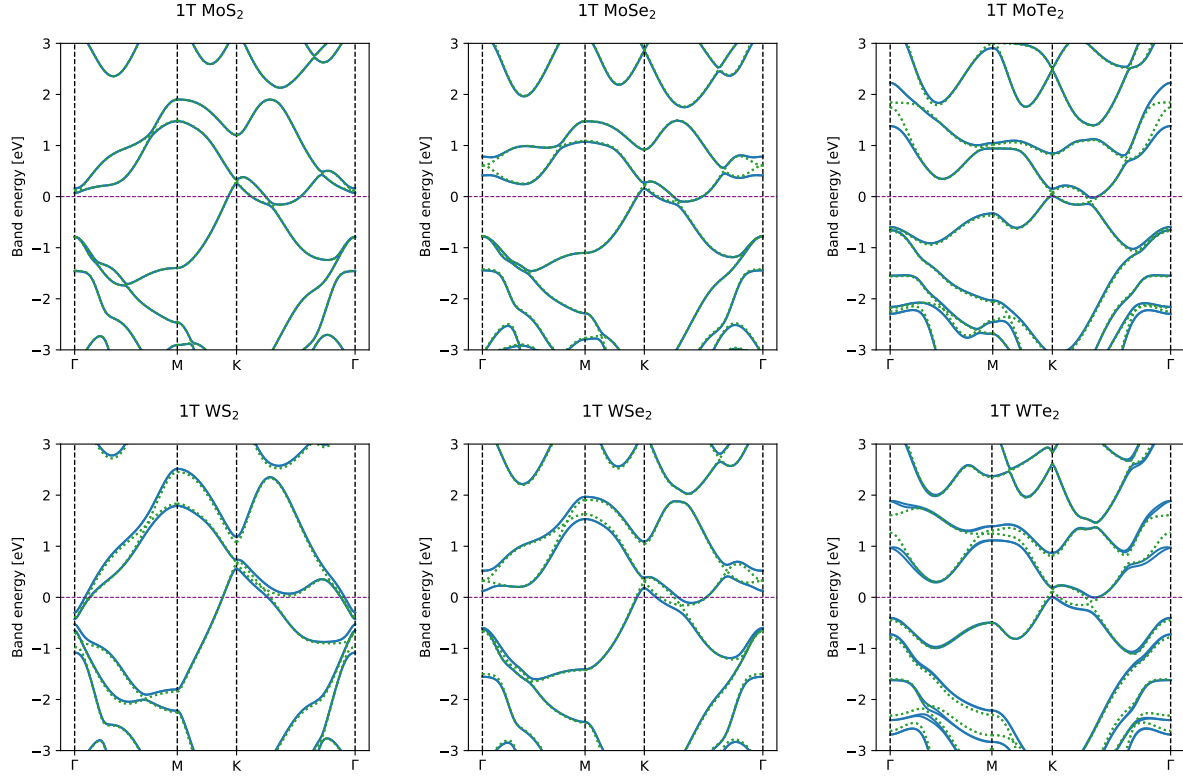


FIG. S2:. Band structures of  $\text{MX}_2$  monolayers in the 1T phase obtained from the RESPECT code at the scalar-relativistic (dashed lines, no SOC) and fully-relativistic (full lines, with SOC) levels of the theory. The horizontal dashed black line marks the Fermi level. The unit-cell structure and lattice parameters were taken from Ref. ? .

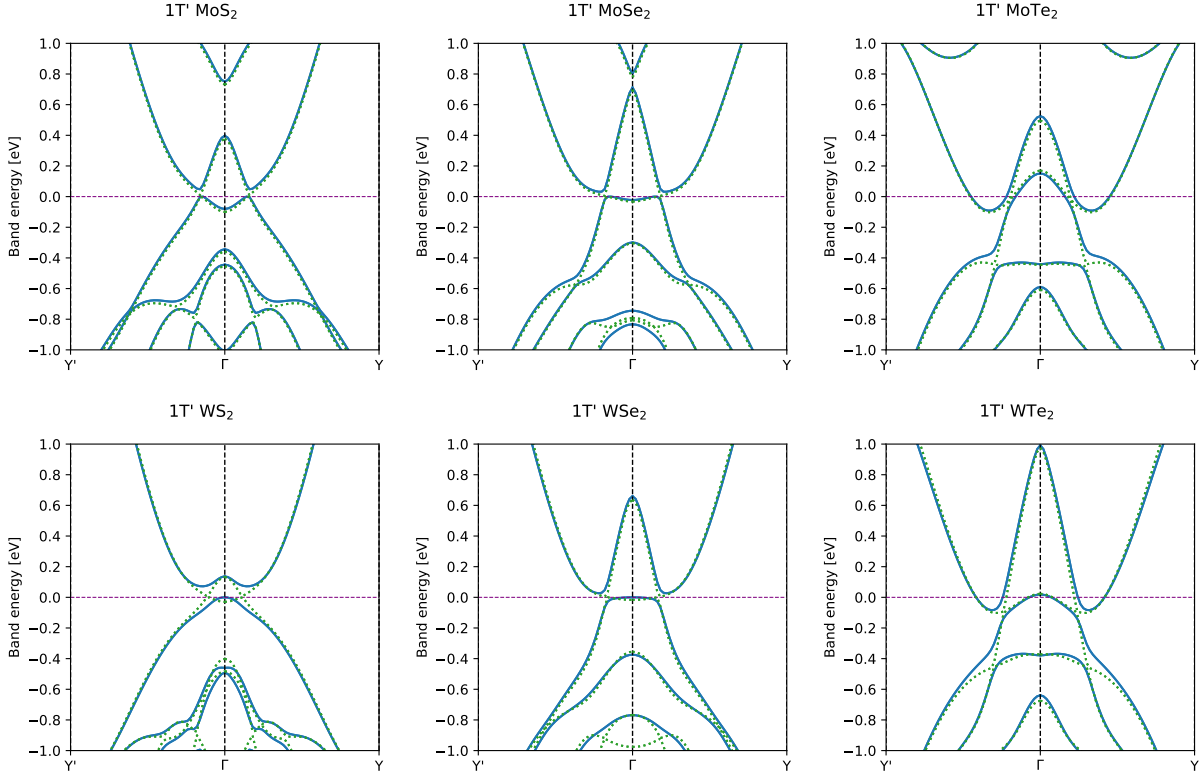


FIG. S3:. Band structures of MX<sub>2</sub> monolayers in the 1T' phase obtained from the RESPECT code at the scalar-relativistic (dashed lines, no SOC) and fully-relativistic (full lines, with SOC) levels of theory. The horizontal dashed black line marks the Fermi level. The unit-cell structure and lattice parameters were taken from Ref. ? .